KU LEUVEN

Citation	Ivo Stassen, Mark Styles, Gianluca Grenci, Hans Van Gorp,Willem Vanderlinden, Steven De Feyter, Paolo Falcaro, Dirk De Vos, Philippe Vereecken and Rob Ameloot **Chemical vapour deposition of zeolitic imidazolate framework thin films** Nature Materials, 2016, 15, 304 - 310
Archived version	Author manuscript: the content is identical to the content of the published paper, but without the final typesetting by the publisher
Published version	http://dx.doi.org/10.1038/nmat4509
Journal homepage	http://www.nature.com/nmat/index.html
Author contact	your email steven.defeyter@kuleuven.be your phone number + *32 (0)16 327921*
IR	url in Lirias https://lirias.kuleuven.be/handle/123456789/521503

(article begins on next page)

Chemical vapour deposition of zeolitic imidazolate framework thin films

Ivo Stassen[1,2], Mark Styles[3], Gianluca Grenci[4], Hans Van Gorp[5], Willem Vanderlinden[5], Steven De Feyter[5], Paolo Falcaro[3], Dirk De Vos[1], Philippe Vereecken[1,2], Rob Ameloot[1*]

[1]Department of Microbial and Molecular Systems, Centre for Surface Chemistry and Catalysis, KU Leuven – University of Leuven, Celestijnenlaan 200F, B-3001 Leuven, Belgium. [2]imec, Kapeldreef 75, B-3001 Leuven, Belgium. [3]CSIRO Manufacturing Flagship, Clayton, Victoria 3168, Australia. [4]MBI, National University of Singapore T-Lab, 5A Engineering Drive 1, Singapore. [5]Department of Chemistry, KU Leuven – University of Leuven, Celestijnenlaan 200F, B-3001 Leuven, Belgium.

[*]To whom correspondence should be addressed: rob.ameloot@biw.kuleuven.be

Abstract: Integrating metal-organic frameworks (MOFs) in microelectronics has disruptive potential because of the unique properties of these microporous crystalline materials. Suitable film deposition methods are crucial to leverage MOFs in this field. Conventional solvent-based procedures, typically adapted from powder preparation routes, are incompatible with nanofabrication because of corrosion and contamination risks. We demonstrate a chemical vapour deposition process (MOF-CVD) that enables high-quality films of ZIF-8, a prototypical MOF material, with a uniform and controlled thickness, even on high-aspect ratio features. Furthermore, we demonstrate how MOF-CVD enables previously inaccessible routes such as lift-off patterning and depositing MOF films on fragile features. The compatibility of MOF-CVD with existing infrastructure, both in research and production facilities, will dramatically facilitate MOF integration in microelectronics. MOF-CVD is the first vapour-phase deposition

method for any type of microporous crystalline network solid and marks a milestone in processing such materials.

Metal-organic frameworks (MOFs) are a rapidly growing class of microporous crystalline coordination polymers that consist of metal-containing nodes connected by multitopic organic linkers[1]. Because of their unique properties, including ultrahigh specific surface areas and a functionalizable pore interior, these materials have the potential to enable disruptive technologies in application areas such as catalysis[2], gas storage[3] and molecular separations[4]. In addition to these application areas, where MOF powders are rapidly approaching commercial viability via established bulk synthesis methods[5], there is tremendous potential for integrating MOFs into microelectronics[6–8], e.g. as active sensor coatings[9], low-k dielectrics[10,11] and tuneable conductors[12]. A key enabling step in leveraging the properties of MOFs in microelectronics will be the development of robust thin film deposition methods[7,8,13]. Thus far, all reported procedures for the deposition of MOF thin films are adaptations of powder preparation methods and typically involve the combination of linkers and metal salts in an organic solvent, often under solvothermal conditions. However, this approach is incompatible with microelectronic fabrication processes since contacting preformed circuitry with a MOF synthesis solution leads to corrosion and chemical contamination. MOF particles formed as a result of homogeneous nucleation in solution pose a further contamination risk. Additionally, the use of solvents, especially under solvothermal conditions, raises safety, processability and cost concerns and is in direct conflict with the 'green fabrication' principles stipulated in the strategic roadmap of the microelectronics industry[14].

Chemical vapour deposition (CVD) is a cornerstone technology in microdevice fabrication[15,16]. This deposition method is based on the reaction of vaporised substances on or nearby a substrate to

form a uniform thin film of precisely controlled thickness. The materials scope of CVD has expanded considerably during the last decade: from metals and inorganics to organic and hybrid materials such as carbon allotropes,[17] organic polymers[18] and hybrid polymers[19]. The primary driver for expanding the CVD materials range is the need for thin films of newly developed high-performance materials to meet the ever more demanding required specifications, for instance in extending Moore's law. In this context, attempts have been undertaken to deposit MOFs using vapour-phase precursors[20,21] or via physical vapour deposition of preformed compounds[22–24], but without exception these have resulted in closely packed coordination polymers without measurable microporosity.

Herein, we demonstrate a CVD approach for producing ZIF-8, zinc-(2-methylimidazolate)$_2$,[25] a member of the widespread zeolitic imidazolate framework (ZIF) subclass of MOFs. The present study is, to the best of our knowledge, the first reported vapour deposition process for any kind of crystalline microporous network solid. The 'MOF-CVD' method consists of two steps: a metal oxide deposition step and a vapour-solid reaction step (Fig. 1). This approach enables the deposition of ZIF-8 thin films with a uniform and controlled thickness, even on high-aspect ratio features. The compatibility of MOF-CVD with existing and scalable fabrication infrastructure, both in research and production facilities, will dramatically facilitate MOF integration in microelectronics and related applications. Furthermore, we demonstrate how MOF-CVD enables previously inaccessible routes such as lift-off patterning and depositing MOF films on fragile features.

Solvothermal transformation of metal oxides has been used to generate two- and three-dimensional MOF patterns[26–28]. However, in addition to the issues of compatibility with

nanofabrication outlined above, the difficulty in using solvothermal oxide-to-MOF transformations for MOF film growth lies in precisely matching the oxide dissolution and MOF crystallisation rates. Due to slight local differences in dissolution rate, coupled with fast diffusion of the released metal ions, the solvothermal transformation approach risks the formation of rough films, pinholes and even homogeneous nucleation of MOF particles in solution. In contrast, in the MOF-CVD approach, such issues are largely avoided by supplying the organic linker as a vapour instead of in solution. Key to the success of the MOF-CVD approach is that ions remain localized, within a nanometre-range diffusion radius, which allows the transformation of ultrathin oxide precursor films with high fidelity.

Of the metal oxide deposition protocols commonly used in nanofabrication, atomic layer deposition (ALD) was selected to control the deposited layer thickness with nanometre precision and to study the effect of precursor film thickness changes on the oxide film conversion efficiency. ALD zinc oxide films with 3-15 nm thickness were transformed to ZIF-8 by exposure to 2-methylimidazole (HmIM) vapour at 100 °C for 30 min, resulting in highly reflective and uniform mirror-finish coatings (Supplementary Fig. 1). X-ray diffraction (XRD) confirms the formation of highly crystalline ZIF-8 (Fig. 2a, Supplementary Fig. 2-4). Attenuated total reflection Fourier transform infrared spectroscopy (ATR-FTIR) further indicates the presence of the linker in its deprotonated 2-methylimidazolate (mIM) form, corresponding to incorporation in the ZIF-8 framework (Supplementary Fig. 5). The ZIF-8 CVD films are continuous and consist of crystallites up to 500 nm in size (Fig. 2b-c, Supplementary Fig. 6-11).

The oxide-to-MOF conversion efficiency was studied for different zinc oxide precursor thicknesses. Cross-sectional analysis via transmission electron microscopy (TEM) indicated

complete transformation of precursor films of less than 10 nm thick (Fig 2d, Supplementary Fig. 12-14). After transformation of such ultrathin precursor films, no residual zinc oxide can be observed at the interface between the formed ZIF-8 film and the substrate via high-magnification TEM (fig 2d, inset). Variations in composition and density within completely and partially transformed zinc oxide films, with an original thickness of 6 and 15 nm respectively, were evaluated by high-angle annular dark field (HAADF) and energy dispersive X-ray spectroscopy (EDS) mapping (Fig. 2e-f). As expected from the low density of the formed ZIF-8 film, the completely transformed zinc oxide layer appears dark. When zinc oxide is still present, a sharp interface is observed between the ZIF-8 film and the residual dense precursor. The EDS maps and profiles further validate the homogeneous composition of the ZIF-8 film and the sharp interface with unaltered underlying oxide layers (Supplementary Fig. 15). The homogeneous distribution of HmIM in the formed ZIF-8 film was confirmed by time-of-flight secondary ion mass spectrometry (TOF-SIMS) depth profiling (Supplementary Fig. 16, 17 and Supplementary Tab. 1). Transformation of dense zinc oxide to highly porous ZIF-8 is expected to cause an expansion in film thickness. The change in interference-based colour upon transformation of optical quality zinc oxide coatings to mirror-finish ZIF-8 films is a first indication of such expansion (Supplementary Fig. 1). Cross-sectional TEM imaging confirms the formation of ZIF-8 films with an average thickness of 52 and 104 nm when fully converting 3 and 6 nm oxide precursor layers, respectively. Remarkably, the 17-fold thickness increase was found to be in striking agreement with the theoretically expected value based on the ratio of the crystallographic volume occupied per mole of zinc in zinc oxide and ZIF-8, namely 14.3 $cm^3\ mol_{Zn}^{-1}$ and 239.9 $cm^3\ mol_{Zn}^{-1}$, respectively. The arithmetic average surface roughness (R_a) of the 104 nm thick film is 24.9 nm,

as measured for a 2 × 2 μm^2 probe area by AFM (Fig. 2c). This surface roughness is estimated to be similar to that of the smoothest ZIF-8 thin films thus far[29–31] and considerably lower than that of those obtained by solvothermal zinc oxide transformation[28]. The substantial increase in roughness relative to the ALD oxide precursor layers is mostly due to the progressive formation of large (up to 500 nm) crystal faces (Supplementary Fig. 18-19). The thickness and surface roughness of the films is significantly smaller than these exposed crystal faces. This observation shows that the ZIF-8 crystal growth during solid-vapour transformation is predominantly confined to the substrate, which underlines the low mobility of the zinc ions released from the zinc oxide precursor film in the absence of a synthesis solvent.

In the previous examples, a 40 nm thick ALD titanium oxide adhesion layer was present underneath the zinc oxide precursor film. The use of an adhesion layer to bridge the substrate and the functional layers deposited on top is common practice in nanofabrication[15]. Comparison between titanium and silicon oxide adhesion layers showed more uniform ZIF-8 MOF-CVD coatings in the former case, in accordance with previous reports on solvothermal ZIF-8 film growth (Supplementary Fig. 20)[32,33]. As an alternative to a dedicated adhesion layer, excess zinc oxide can be deposited to ensure a good bond between the formed ZIF-8 film and the substrate, since partial conversion of this precursor leaves an oxide bridging layer.

In addition to excellent control over thickness, ALD permits highly conformal coatings, even on high aspect-ratio features.[34] To illustrate that similar conformality can be achieved in the MOF-CVD process, ZIF-8 was deposited on 25:1 aspect ratio silicon pillars by vapour-solid transformation of 25 nm ALD zinc oxide films. The resulting ZIF-8 thin films displayed a homogeneous coverage of the pillars (Fig. 3a-d). Krypton physisorption was selected to directly

measure the generated ZIF-8 porosity after different vapour-solid reaction times because of the superior accuracy of this technique over nitrogen and argon volumetric adsorption measurements[35]. The type I shape of these isotherms (fig 3e), showing adsorption and saturation in the low pressure range, corresponds to filling of the ZIF-8 micropores[36]. The Brunauer-Emmett-Teller (BET) specific surface area, expressed per film area, was found to be 41, 74 and 88 $m^2 m^{-2}$ for reaction times of 15, 30 and 45 min, respectively. Evaluating these physisorption data against the calculated ZIF-8 internal surface for Kr probing (1299 $m^2 cm^{-3}$ for 0.185 nm probe radius[37]), results in an average thickness of the microporous MOF film of 32, 59 and 69 nm after 15, 30 and 45 min reaction times, respectively. The excellent agreement of these values with cross-sectional electron microscopy thickness measurements further confirms the MOF film homogeneity and conformality (Supplementary Fig. 21).

Depositing ultrathin conformal MOF-CVD coatings on high-aspect ratio features enables a dramatic improvement in adsorption kinetics compared to MOF films on a flat substrate. Fig. 3f shows a comparative single-pulse Kr adsorption experiment between flat and pillar array substrates, coated with a 2500 and 85 nm ZIF-8 film, respectively. Even though both MOF-coated substrates have identical equilibrium adsorption capacities (Supplementary Fig. 22), equilibrium is reached within 5 min for the MOF-CVD coated high-aspect ratio sample but not for several hours for the flat film deposited via a reported procedure[27].

The sequence of Kr adsorption isotherms in Fig. 3e indicates that the ZIF-8 growth rate decreases with time, as the additional uptake capacity generated during 15 min reaction time increments decreases. Similar self-inhibiting growth when starting from thick zinc oxide films, has also been observed in the formation of ZIF-8 via solvothermal oxide-to-MOF transformations and is related

to diffusion limitations, of the organic linker to the oxide and/or of zinc species to the growing crystal interface[28]. Nevertheless, as discussed above, full conversion of sufficiently thin oxide layers to ZIF-8 is possible (Fig. 2d). Re-exposing the ZIF-8 coated pillar arrays to a second HmIM vapour treatment, and repeating Kr adsorption measurements for the same substrates, provides additional mechanistic insights (Supplementary Fig. 23 and Supplementary Tab. 2). Firstly, the isotherm and BET specific surface area remains unaffected for the thicker ZIF-8 films previously formed during 30-45 min reactions, in accordance with ZIF-8 acting as a diffusion barrier. Secondly, the thinnest ZIF-8 film, initially formed after 15 min of reaction, showed a significant increase in uptake, which indicates that zinc oxide conversion can still take place below a certain ZIF-8 film thickness. However, exposing the substrate twice for 15 min resulted in a 20 % lower BET surface area than a single 30 min exposure. This observation evidences that once stopped, the reaction cannot be immediately restarted and continued at the same rate.

To further elucidate the neutralisation reaction between zinc oxide and HmIM vapour and the resulting ZIF-8 crystallisation (Fig. 4a), *in situ* powder X-ray diffraction (PXRD) experiments were performed on a physical mixture of both reactants, heated below the HmIM melting temperature (Supplementary Fig. 24-27). No phases other than HmIM, zinc oxide and ZIF-8 are detected at any time (Fig. 4b). Note, however, that HmIM undergoes a phase transition when heated above ~80°C. The space group of this unreported high temperature phase (HT-HmIM) was indexed as *Fdd2*, with lattice parameters a = 16.278 Å, b = 12.605 Å, and c = 4.894 Å (Supplementary section 15).

Under vapour-solid reaction conditions, the ZIF-8 mass fraction in the mixture increases sigmoidally as a function of time (Fig. 4c). The slope of this curve, *i.e.* the crystallisation rate, levels off after an initial onset period. This levelling off can be explained by the crystallisation of a

continuous ZIF-8 film that covers the zinc oxide particles and acts as a diffusion barrier, for both HmIM towards the metal oxide and zinc species towards the growing crystallites. Interestingly, an increased reaction temperature results in levelling off of the crystallization rate after a comparable reaction time, although a much higher ZIF-8 mass fraction is formed (Fig 4c and Supplementary section 14). This indicates that the neutralisation reaction front has progressed deeper into the zinc oxide, thus mobilising more Zn^{2+} for MOF formation, before nucleation and growth of a continuous ZIF-8 film. This observation can be attributed to the faster neutralisation reaction kinetics and to the faster diffusion and increased vapour pressure of HmIM (from 267 Pa at 115 °C to 830 Pa at 130 °C)[38] at higher temperatures. Accordingly, thicker ZIF-8 films are observed when thick zinc oxide films are partially transformed at higher temperatures (Supplementary Fig. 30).

Crystallisation of the highly porous ZIF-8 framework in the absence of structure-directing additives or solvents seems remarkable at first sight. Thermodynamic simulations, however, have shown that the neutralisation reaction between zinc oxide and HmIM is energetically favourable in the case of ZIF-8 formation and largely driven by the stabilisation of the zinc coordination sphere, with replacement of Zn-O by Zn-N bonds, and by the formation of water[39]. It is our hypothesis that the continuous formation of water as a neutralisation product at the reaction interface plays a central role in the ZIF-8 crystallisation during MOF-CVD. This proposition is based on the observation that the rate of ZIF-8 formation increases when the *in situ* XRD experiment is performed in a humid nitrogen gas flow, in comparison to a dry flow (Fig. 4d). A possible explanation for this behaviour is that water retained at the reaction interface results in the formation of a liquid-like layer which renders the MOF building blocks sufficiently mobile to

enable crystallisation. However, because of the elevated MOF-CVD process temperature and the hydrophobicity of the formed ZIF-8 layer, there is a strong driving force for the generated water to evaporate. Decreasing or increasing the dehydration rate, by performing the oxide-to-MOF transformation under a humid or dry nitrogen gas flow respectively, is therefore expected to have a direct effect on the MOF crystallization rate. This hypothesis is further supported by the observation that after halting the oxide-to-MOF transformation, resulting in full dehydration and immobilisation of the surface layer, the conversion reaction cannot be readily resumed by reintroducing the sample into the reactive atmosphere. The mechanism of the MOF-CVD process therefore has parallels with the steam-assisted synthesis protocols described for some MOFs and zeolites[40,41]. Additionally, water may serve as a catalyst in the zinc oxide neutralisation reaction, by protonation of the organic linker[42] and by hydration of zinc oxide. Growth of a non-porous diamondoid (*dia*) $Zn(mIM)_2$ polymorph has previously been observed during oxide-to-MOF transformations at high water concentrations[40,43,44]. Because of the continuous removal of water generated during MOF-CVD of ZIF-8 formation of this material is avoided.

Exploratory experiments with altered metals and linkers were performed to demonstrate the general applicability of the MOF-CVD approach. Related materials such as ZIF-61, ZIF-67 and ZIF-72 were deposited under similar experimental conditions as ZIF-8 (Supplementary Fig. 31-34). Moreover, the applicability of MOF-CVD to chemistries very different from ZIFs is demonstrated by the transformation of copper hydroxide films to previously reported crystalline Cu(II)-dicarboxylates through vapour-solid reaction (Supplementary Fig. 35-36). A future direction for MOF-CVD research will be to steer towards porous network topologies.

MOF-CVD will dramatically facilitate the integration of MOF materials in microelectronic devices by routes that were previously not accessible. As a first demonstration case, we selected additive lithography, commonly referred to as lift-off patterning, which is an essential method in manufacturing organic and large area electronics. In lift-off patterning, a lithographically patterned photoresist is used as a mask during vapour-phase material deposition and subsequently removed, leaving patterned features of the deposited material (Fig. 5a). Since photoresist removal in the last step of the lift-off process is typically performed in a polar organic solvent, it is hard to keep suitable resist materials from swelling and/or dissolving in typical MOF synthesis solutions. In contrast, since MOF-CVD is completely solvent-free, there is no risk of distorting the photoresist and losing pattern reproduction fidelity. An exemplary pattern manufactured by MOF-CVD in combination with the lift-off methodology is shown in Fig. 5b-c. In this case, zinc oxide was deposited by directional reactive sputtering instead of by ALD, indicating the flexibility of the oxide deposition step in MOF-CVD. Note that these 1.7 μm wide rings are the highest resolution and thinnest photolithographically defined MOF patterns to date (Supplementary Fig. 37)[45–47]. In a second demonstration case, features too fragile to withstand the capillary forces during solvent processing are conformally coated directly via MOF-CVD. Functionalized elastomeric pillar arrays, typically fabricated via soft lithography (fig 5d), are used in a wide range of applications where stimulated collapse plays a crucial role; e.g. stem cell stimulation[48], microfluidic sensing[49] and biomimetic adhesives[50]. Such pillars can be coated by MOF-CVD without affecting the structural integrity of the arrays (Fig. 5e and Supplementary Fig. 38). For comparison, a widely used solution phase method for ZIF-8 deposition[51] resulted in undesired collapse of the pillars, resulting in loss of the original micropattern features (Fig. 5f).

In summary, these results demonstrate a deposition process for ultrathin, homogeneous and conformal MOF films via vaporised precursors. We believe that further development of the MOF-CVD method, inspired by the recent advances in CVD of hybrid materials[19], will lead towards unmatched control over film features such as orientation, thickness and surface roughness. Furthermore, an extension towards MOFs consisting of a broad range of metals and ligands is feasible based on exploratory experiments. The compatibility of the solvent-free MOF-CVD process with existing microfabrication processes and infrastructure will considerably expedite the integration of MOF materials in microelectronics and related applications requiring e.g. state-of-the-art low dielectric constant[30], low refractive index[45] or low density/high surface area[51] materials. Moreover, as MOF-CVD is the first example of vapour-phase deposition of any type of microporous crystalline network solid, the current results mark an important milestone in the processing of such materials.

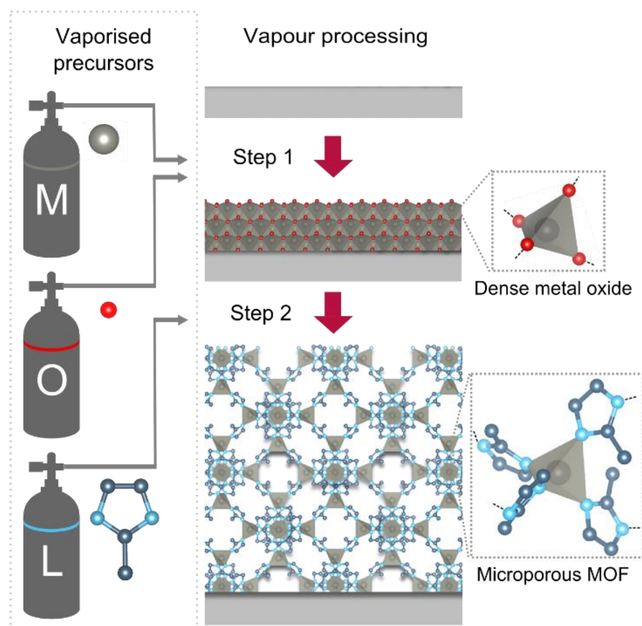

Figure 1 | Chemical vapour deposition of ZIF-8 thin films. The procedure consists of a metal oxide vapour deposition (Step 1) and a consecutive vapour-solid reaction (Step 2). Metal, oxygen and ligand sources are labelled as M, O and L, respectively. Metal oxide deposition can be achieved by atomic layer deposition (M, diethylzinc; O, oxygen/water) or by reactive sputtering (M, zinc; O, oxygen plasma). Atom colours: zinc (grey) oxygen (red), nitrogen (light blue) and carbon (dark blue); hydrogen atoms are omitted for clarity.

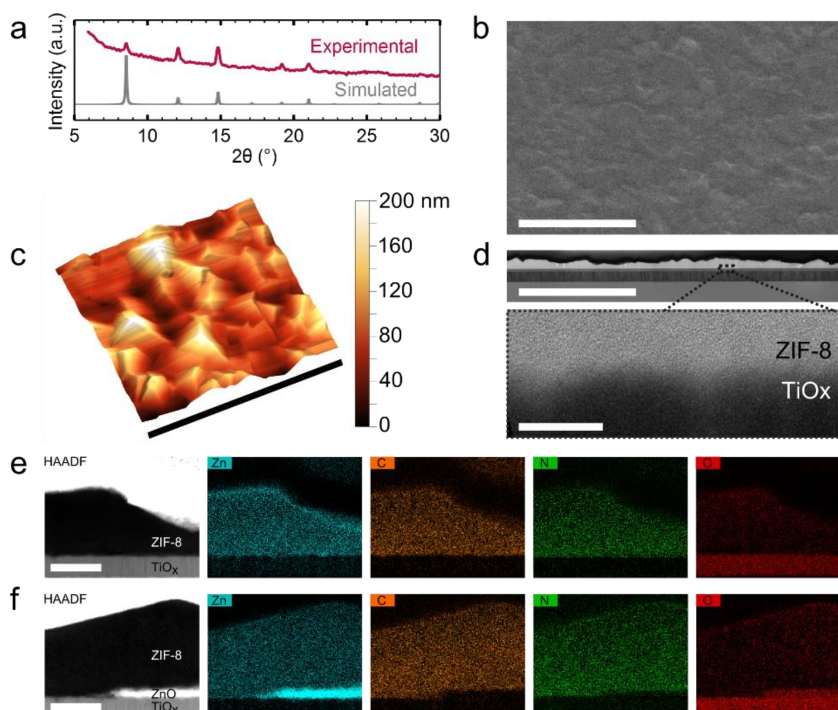

Figure 2 | Characterization of chemical vapour deposited ZIF-8 thin films. a, X-ray diffraction pattern of a ZIF-8 CVD film and simulated pattern for ZIF-8. **b**, Scanning electron microscopy top view. **c**, 3D rendered AFM topograph. **d**, Focused-ion beam TEM cross section. Inset: high-resolution magnification of the interface between ZIF-8 and the titanium oxide substrate. **e**, HAADF and EDS cross section maps of a completely transformed film. **f,** HAADF and EDS cross section maps of a partially transformed film. The completely transformed film (a-e) was obtained by vapour-solid reaction of a 6 nm thick ALD zinc oxide film. The partially transformed film (f) was obtained by vapour-solid reaction of a 15 nm thick ALD zinc oxide film. Scale bars: 2 µm for panels b-d, 20 nm for inset, 100 nm for e-f.

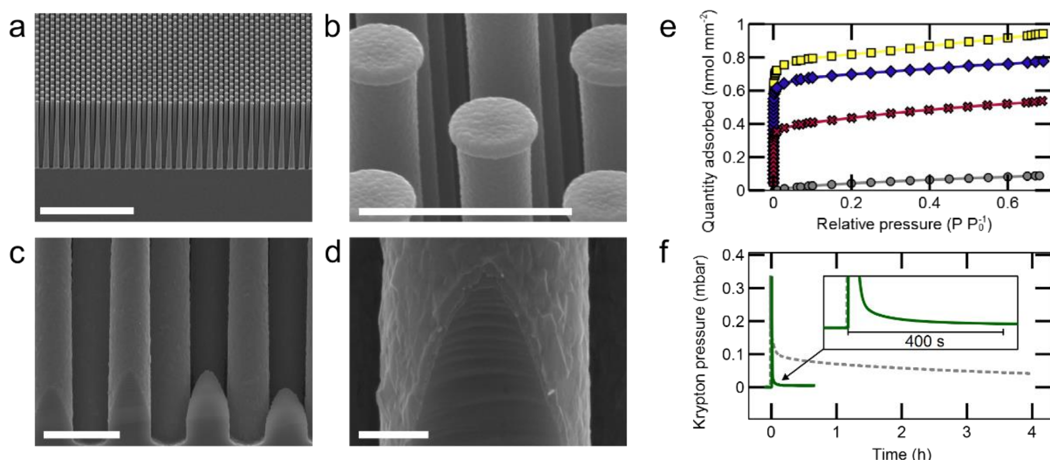

Figure 3 | Conformal ZIF-8 thin films deposition on high aspect ratio pillar arrays. a-b, Scanning electron microscopy images showing the ZIF-8 coated silicon pillar array. **c-d,** High-magnification scanning electron microscopy images displaying the homogeneous coverage at the base of the pillars. **e,** Kr adsorption isotherms for the zinc oxide coated pillar array (grey circles) and after 15 min (red crosses), 30 min (blue diamonds) and 45 min (yellow squares) vapour-solid reaction. **f,** Single-pulse Kr adsorption kinetics experiment for a 85 nm thick high aspect ratio ZIF-8 film (green) and a 2500 nm thick flat film (dashed, grey). Scale bars: 50 µm for panel a, 5 µm for b-c and 1 µm for d.

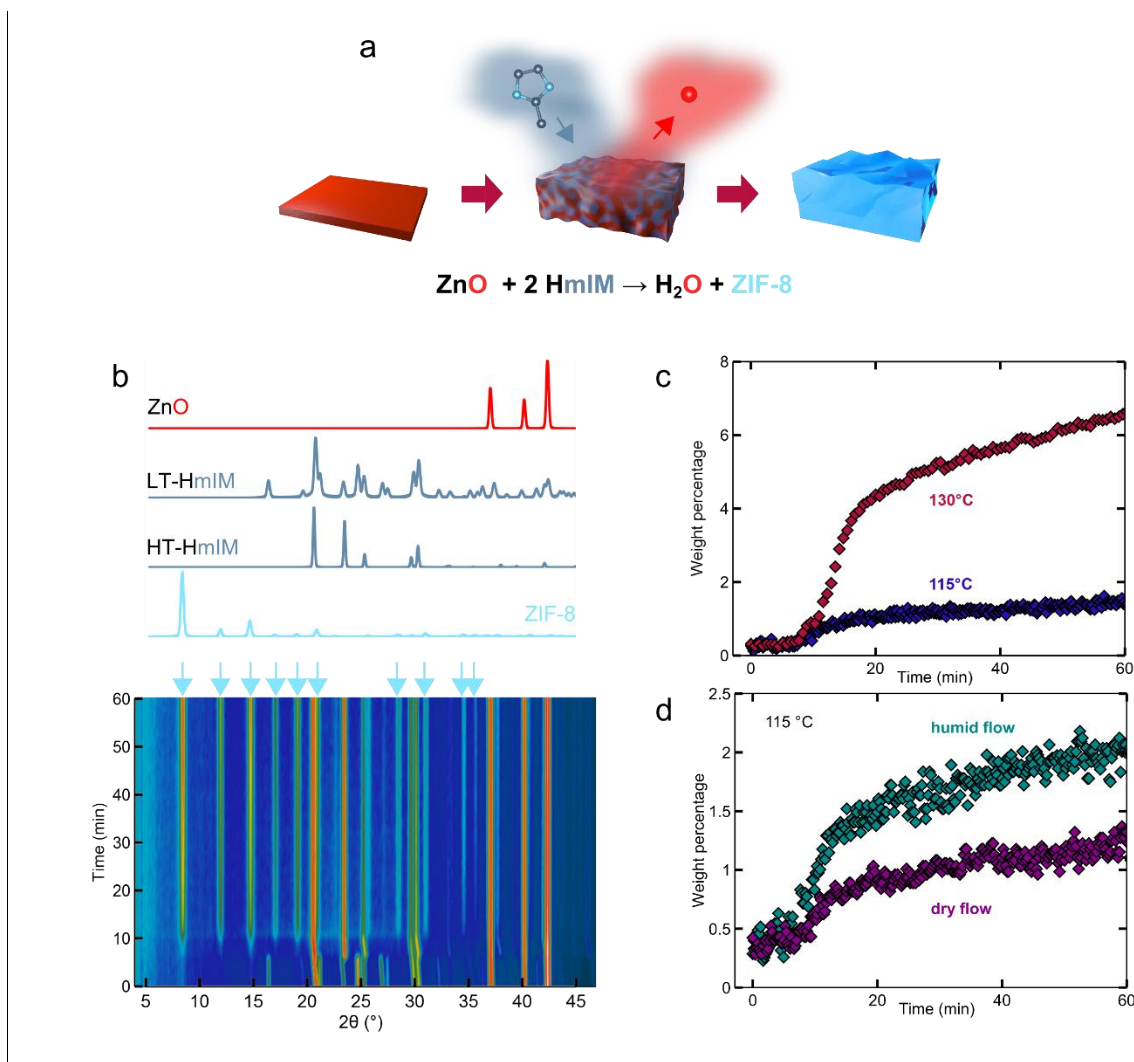

Figure 4 | Vapour-solid reaction of zinc oxide and HmIM studied by *in situ* powder X-ray diffraction (PXRD). a, Schematic overview of the transformation mechanism. **b,** Plot of the time-resolved diffraction patterns viewed down the intensity axis, showing the transformation of crystalline phases in a 1:2 mixture of crystalline zinc oxide and HmIM powder at 130°C. Colour scale from blue (low intensity) to red (high intensity). Simulated pure-phase diffraction patterns are plotted at the top for reference and peaks corresponding to ZIF-8 are highlighted by the blue arrows. **c,** ZIF-8 phase quantification for *in situ* reaction experiments at 115 °C (blue) and 130 °C (red). **d,** ZIF-8 phase quantification for *in situ* reaction experiments at 115 °C under a continuous

dry nitrogen flow (purple) and a nitrogen flow humidified to 33 % relative humidity at room temperature (green).

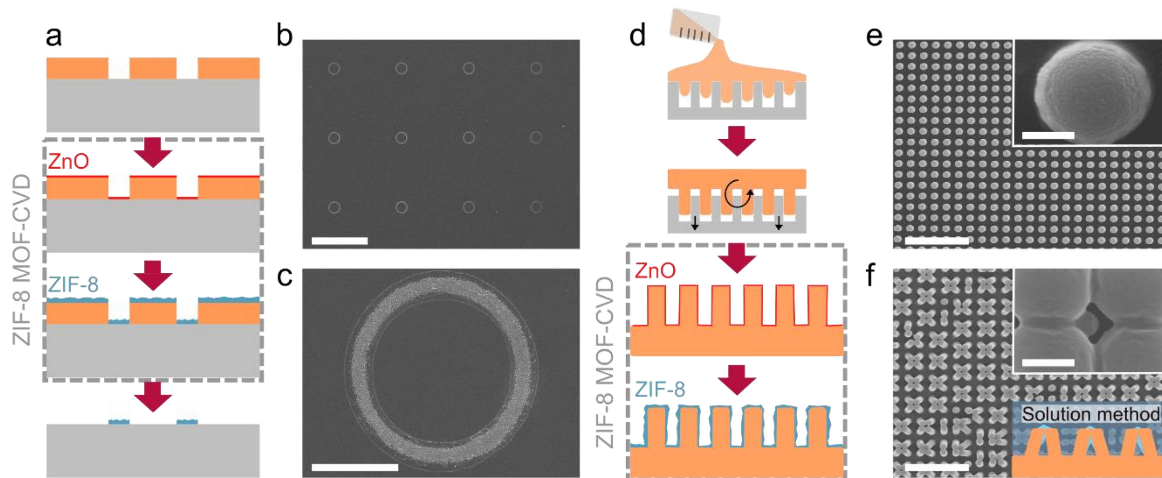

Figure 5 | MOF integration routes enabled by the MOF-CVD process: lift-off patterning and coating of fragile features. a, Schematic diagram of MOF pattern deposition by MOF-CVD and subsequent lift-off of a patterned photoresist . **b-c,** Scanning electron microscopy images of the manufactured ZIF-8 patterns. **d,** Schematic diagram of the production of ZIF-8 coated polydimethylsiloxane pillars by soft-lithography and MOF-CVD. **e,** Scanning electron microscopy image of MOF-CVD coated PDMS pillars. **f,** Scanning electron microscopy image of identical PDMS pillars after conventional solution processing of ZIF-8. The MOF-CVD processing steps are indicated with a dashed line in panels a and d. Oxide and MOF films are represented in red and blue, respectively. Scale bars: 100 µm for panel b, 10 µm for c, 20 µm for e-f, 1 µm for insets.

References

1. Furukawa, H., Cordova, K. E., O'Keeffe, M. & Yaghi, O. M. The chemistry and applications of metal-organic frameworks. *Science* **341,** 1230444 (2013).

2. Liu, J. *et al.* Applications of metal-organic frameworks in heterogeneous supramolecular catalysis. *Chem. Soc. Rev.* **43,** 6011–6061 (2014).

3. Wilmer, C. E. *et al.* Large-scale screening of hypothetical metal–organic frameworks. *Nat. Chem.* **4,** 83–89 (2011).

4. Li, J.-R., Sculley, J. & Zhou, H.-C. Metal–Organic Frameworks for Separations. *Chem. Rev.* **112,** 869–932 (2011).

5. Peplow, M. Materials science: The hole story. *Nature* **520,** 148–150 (2015).

6. Bétard, A. & Fischer, R. A. Metal-organic framework thin films: from fundamentals to applications. *Chem. Rev.* **112,** 1055–83 (2012).

7. Falcaro, P. *et al.* MOF positioning technology and device fabrication. *Chem. Soc. Rev.* **43,** 5513–60 (2014).

8. Stavila, V., Talin, A. A. & Allendorf, M. D. MOF-based electronic and opto-electronic devices. *Chem. Soc. Rev.* **43,** 5994–6010 (2014).

9. Kreno, L. E. *et al.* Metal-organic framework materials as chemical sensors. *Chem. Rev.* **112,** 1105–25 (2012).

10. Baklanov, M. R., Adelmann, C., Zhao, L. & De Gendt, S. Advanced Interconnects: Materials, Processing, and Reliability. *ECS J. Solid State Sci. Technol.* **4,** Y1–Y4 (2014).

11. Usman, M., Mendiratta, S. & Lu, K.-L. Metal-Organic Frameworks: New Interlayer Dielectric Materials. *ChemElectroChem* **2,** 786–788 (2015).

12. Talin, A. A. *et al.* Tunable Electrical Conductivity in Metal-Organic Framework Thin-Film Devices. *Science (80-.).* **343,** 66–69 (2014).

13. Allendorf, M. D., Schwartzberg, A., Stavila, V. & Talin, A. A. A roadmap to implementing metal-organic frameworks in electronic devices: challenges and critical directions. *Chemistry* **17,** 11372–88 (2011).

14. Semiconductor Industry Association. *The International Technology Roadmap for Semiconductors*. (2013).

15. Pierson, H. O. *Handbook of Chemical Vapor Deposition*. (1997).

16. Martin, P. M. *Handbook of Technologies for Films and Coatings*. (2005).

17. Hirsch, A. The era of carbon allotropes. *Nat. Mater.* **9,** 868–871 (2010).

18. Coclite, A. M. *et al.* 25th Anniversary Article: CVD polymers: A new paradigm for surface modification and device fabrication. *Adv. Mater.* **25,** 5392–5423 (2013).

19. Lee, B. H., Yoon, B., Abdulagatov, A. I., Hall, R. a. & George, S. M. Growth and properties of hybrid organic-inorganic metalcone films using molecular layer deposition techniques. *Adv. Funct. Mater.* **23,** 532–546 (2013).

20. Salmi, L. D. *et al.* Studies on atomic layer deposition of MOF-5 thin films. *Microporous Mesoporous Mater.* **182,** 147–154 (2013).

21. Kojima, T., Choi, W. & Kawano, M. Single-crystal growth of coordination networks via the gas phase and dependence of iodine encapsulation on the crystal size. *Chem. Commun.* **50,** 13793–13796 (2014).

22. Welte, L. *et al.* Organization of coordination polymers on surfaces by direct sublimation. *Adv. Mater.* **21,** 2025–2028 (2009).

23. Fischer, D., Meyer, L. V, Jansen, M. & Müller-Buschbaum, K. Highly Luminescent Thin Films of the Dense Framework (3) ∞ [EuIm2] with Switchable Transparency Formed by Scanning Femtosecond-Pulse Laser Deposition. *Angew. Chem. Int. Ed.* **53,** 706–10 (2014).

24. Meyer, L. V. *et al.* Organic melt, electride, and CVD induced in situ deposition of luminescent lanthanide imidazolate MOFs on nanostructured alumina. *Inorg. Chem. Front.* **2,** 237–245 (2015).

25. Park, K. S. *et al.* From the Cover: Exceptional chemical and thermal stability of zeolitic imidazolate frameworks. *Proc. Natl. Acad. Sci.* **103,** 10186–10191 (2006).

26. Reboul, J. *et al.* Mesoscopic architectures of porous coordination polymers fabricated by pseudomorphic replication. *Nat. Mater.* **11,** 717–23 (2012).

27. Stassen, I. *et al.* Solvent-free synthesis of supported ZIF-8 films and patterns through transformation of deposited zinc oxide precursors. *CrystEngComm* **15,** 9308 (2013).

28. Khaletskaya, K. *et al.* Self-directed localization of ZIF-8 thin film formation by conversion of ZnO nanolayers. *Adv. Funct. Mater.* **24,** 4804–4811 (2014).

29. Hou, C., Xu, Q., Peng, J., Ji, Z. & Hu, X. (110)-Oriented ZIF-8 Thin Films on ITO with Controllable Thickness. *ChemPhysChem* **14,** 140–144 (2013).

30. Eslava, S. *et al.* Metal-Organic Framework ZIF-8 Films As Low-κ Dielectrics in Microelectronics. *Chem. Mater.* **25,** 27–33 (2013).

31. Shekhah, O. & Eddaoudi, M. The liquid phase epitaxy method for the construction of oriented ZIF-8 thin films with controlled growth on functionalized surfaces. *Chem. Commun.* **49,** 10079–81 (2013).

32. Bux, H. *et al.* Zeolitic Imidazolate Framework Membrane with Molecular Sieving Properties by Microwave-Assisted Solvothermal Synthesis. *J. Am. Chem. Soc.* **131,** 16000–16001 (2009).

33. Bux, H., Chmelik, C., Van Baten, J. M., Krishna, R. & Caro, J. Novel MOF-membrane for molecular sieving predicted by IR-diffusion studies and molecular modeling. *Adv. Mater.* **22,** 4741–4743 (2010).

34. Johnson, R. W., Hultqvist, A. & Bent, S. F. A brief review of atomic layer deposition: From fundamentals to applications. *Mater. Today* **17,** 236–246 (2014).

35. Thommes, M. & Cychosz, K. a. Physical adsorption characterization of nanoporous materials: Progress and challenges. *Adsorption* **20,** 233–250 (2014).

36. Rouquerol, F., Rouquerol, J. & Sing, K. *Adsorption by Powders and Porous Solids*. (1999).

37. Nezbeda, I. & Aim, K. Perturbed hard-sphere equations of state of real fluids. II. Effective hard-sphere diameters and residual properties. *Fluid Phase Equilib.* **17,** 1–18 (1984).

38. Jiménez, P., Roux, M. V. & Turrión, C. Thermochemical properties of N-heterocyclic compounds IV. Enthalpies of combustion, vapour pressures and enthalpies of sublimation, and enthalpies of formation of 2-methylimidazole and 2-ethylimidazole. *J. Chem. Thermodyn.* **24,** 1145–1149 (1992).

39. Hughes, J. T., Bennett, T. D., Cheetham, A. K. & Navrotsky, A. Thermochemistry of Zeolitic Imidazolate Frameworks of Varying Porosity. *J. Am. Chem. Soc.* **135,** 598–601 (2013).

40. Shi, Q., Chen, Z., Song, Z., Li, J. & Dong, J. Synthesis of ZIF-8 and ZIF-67 by steam-assisted conversion and an investigation of their tribological behaviors. *Angew. Chem. Int. Ed.* **50,** 672–5 (2011).

41. Meng, X. & Xiao, F. S. Green routes for synthesis of zeolites. *Chem. Rev.* **114,** 1521–1543 (2014).

42. Mottillo, C. *et al.* Mineral neogenesis as an inspiration for mild, solvent-free synthesis of bulk microporous metal–organic frameworks from metal (Zn, Co) oxides. *Green Chem.* **15,** 2121 (2013).

43. Cliffe, M. J., Mottillo, C., Stein, R. S., Bučar, D.-K. & Friščić, T. Accelerated aging: a low energy, solvent-free alternative to solvothermal and mechanochemical synthesis of metal–organic materials. *Chem. Sci.* **3,** 2495 (2012).

44. Qi, F., Stein, R. S. & Friščić, T. Mimicking mineral neogenesis for the clean synthesis of metal–organic materials from mineral feedstocks: coordination polymers, MOFs and metal oxide separation. *Green Chem.* **16,** 121–132 (2013).

45. Lu, G., Farha, O. K., Zhang, W., Huo, F. & Hupp, J. T. Engineering ZIF-8 thin films for hybrid MOF-based devices. *Adv. Mater.* **24,** 3970–4 (2012).

46. Doherty, C. M. *et al.* Combining UV lithography and an imprinting technique for patterning metal-organic frameworks. *Adv. Mater.* **25,** 4701–4705 (2013).

47. Keitz, B. K., Yu, C. J., Long, J. R. & Ameloot, R. Lithographic deposition of patterned metal-organic

framework coatings using a photobase generator. *Angew. Chemie - Int. Ed.* **53,** 5561–5565 (2014).

48. Migliorini, E. *et al.* Acceleration of neuronal precursors differentiation induced by substrate nanotopography. *Biotechnol. Bioeng.* **108,** 2736–46 (2011).

49. Paek, J. & Kim, J. Microsphere-assisted fabrication of high aspect-ratio elastomeric micropillars and waveguides. *Nat. Commun.* **5,** 3324 (2014).

50. Lee, H., Lee, B. P. & Messersmith, P. B. A reversible wet/dry adhesive inspired by mussels and geckos. *Nature* **448,** 338–341 (2007).

51. Lu, G. & Hupp, J. Metal-organic frameworks as sensors: a ZIF-8 based Fabry-Pérot device as a selective sensor for chemical vapors and gases. *J. Am. Chem. Soc.* **132,** 7832–7833 (2010).

Methods

Substrates. For surface functionalisation, and to serve as internal standard materials during elemental mapping, a stack of titanium based layers ending in titanium oxide was deposited between the silicon wafer support and the zinc oxide layer. These titanium oxide substrate stacks were prepared by respectively sputtering of titanium (15 nm), titanium nitride chemical vapour deposition (140 nm) and titanium oxide ALD (40 nm) on silicon wafers. Silicon dioxide reference substrates were prepared by wet oxidation of silicon wafers. Silicon pillars (staggered square array with pillar diameter of 2 µm, pillar height 50 µm and inter pillar distance of 2 µm) were produced by means of reactive ion etching (Bosch process) using 600 nm silicon oxide patterned by photolithography as the hard mask.

Zinc oxide precursor film deposition. Zinc oxide precursor films were deposited using an ASM EmerALD module. ALD was conducted at 240°C using diethylzinc and oxygen plasma as precursors (500 ms pulse times and 2000 ms purge times; 1.3 mbar reactor pressure). Zinc oxide thicknesses were verified by step-edge profilometry and ellipsometry. For lift-off patterning, zinc oxide sputtering was chosen instead of ALD because of its directionality; this deposition was performed using a NEXX Nimbus 310 module.

ZIF-8 vapour-solid reaction. ZIF-8 vapour-solid reactions were performed in three steps. Firstly, the zinc oxide coated substrate and a closed reactor vessel containing a powder bed of 2-methylimidazole (HmIM) were preheated, separately, at 100 °C. In a second step, the substrate was suspended, top-down, in the reactor vessel, 5 cm above the HmIM powder bed. The vessel was quickly closed and placed for 30 minutes at 100°C. Lastly, the substrate was removed from the bottle while still at 100°C and subsequently activated on a hot plate at 110 °C under a nitrogen flow for 10 minutes. The HmIM powder bed was reused for all reactions.

X-ray diffraction. XRD patterns were collected from both the ZnO precursor and ZIF-8 films using a PANalytical X'Pert PRO Multi-Purpose Diffractometer, fitted with a Co target tube and operated at 40 kV

and 40 mA. The incident beam was defined using a 1/8° fixed divergence slit and 2.3° Soller slits. In the diffracted beam, a graphite monochromator (used to minimise unwanted wavelengths including the Co Kβ signal) was fitted in front of the small, linear position-sensitive detector. Data were collected between 6 and 75° 2θ with a step size of 0.033° 2θ using conventional Bragg-Brentano diffraction geometry[52].

Infrared spectroscopy. ATR-FTIR spectra were recorded on a Varian 670 FTIR spectrometer coupled to a Varian 620 infrared microscope equipped with a slide-on Ge ATR tip.

Electron microscopy and elemental mapping. SEM images were recorded using a Philips XL30 FEG. The samples were sputter coated with 5 nm of Pt before the analysis. TEM **s**amples were coated with a Pt or Pt/Al capping layer by sputtering. Cross section specimens were prepared by FIB lift-out using a FEI Nova600i dual beam system. TEM was executed using a FEI Tecnai F30 scanning microscope equipped with a FEG electron source operated at 300 kV, an EDS and a HAADF detector. Average thickness estimations were obtained using the Fiji distribution[53] of the ImageJ 1.48 software: the surface area of the cross sections was first calculated and subsequently divided by the lateral length to obtain the average film thickness.

Atomic force microscopy. AFM topography images (4 μm^2, 1024 × 1024 pixels, pixel size ~2 nm) were recorded in intermittent contact modus using an Asylum Research Cypher ES AFM instrument. Silicon tips (AC160TS-R3; drive frequency 200-400 kHz) were used. Data analysis (first order least mean square background correction, arithmetic (R_a) and root mean squared (R_q) surface roughness calculations) was performed using the SPIP 6.0.2 and Gwyddion 2.39 software[54].

Time of flight secondary ion mass spectrometry. TOF-SIMS analyses were measured with a TOFSIMS IV instrument from ION-TOF GmbH. Positive ion profiles were measured in a dual beam configuration using a Bi^{3+} (25kV) gun for analysis and a O^{2+} (500eV) gun for sputtering.

Krypton physisorption porosimetry. Krypton adsorption isotherms at 77 K were measured using a Micromeritics 3Flex 3500 gas physisorption instrument. The samples were degassed before measurement at 373 K under vacuum (10^{-2} mbar) for 1 h. Gas uptake equilibria were measured between 10^{-5} and 2.15 mbar (deposition saturation pressure, $P_{0,solid}$). As adsorption of liquid-like multilayers is assumed in the BET theory, the extrapolated condensation saturation pressure of the supercooled liquid ($P_{0,liquid}$ ~ 3.3 mbar) was used as P_0 for isotherm plotting and BET calculations. The BET method was applied in the region between 0.005 and 0.05 P/P_0 for the ZIF-8 coated samples and in the region between 0.05 and 0.2 P/P_0 for a reference zinc oxide coated sample. A krypton adsorptive cross-sectional area of 0.210 nm^2 was assumed for the BET calculations. The BET specific surface area of the samples was corrected for the area of the silicon array support and the sample tube by subtraction of the area of a reference measurement. The calculated surface area of ZIF-8 was obtained by Monte Carlo sampling using Zeo++[55]. The krypton hard sphere radius at the triple point[37], 185 pm, was used as an approximation for the krypton probe radius at 77 K. The single pulse time-resolved experiment was conducted by pulsing a single gas dose to the samples (0.34 mbar, corresponding to 1.3 µmol) and monitoring the pressure in the sample tube decrease over time. The flat film was prepared using our previously reported melt transformation method (1 µm zinc oxide precursor film, 10 min synthesis time)[27].

***In situ* powder X-ray diffraction**. *In situ P*XRD experiments were performed on an INEL diffractometer utilising a CPS120 curved position sensitive detector, capable of collecting 120° 2θ of diffraction data simultaneously. The diffractometer was fitted with a Co long-line focus tube operated at 40 kV and 35 mA. A curved graphite incident beam monochromator was used, and the samples were studied in Debye-Scherrer transmission geometry[52]. Data were collected continuously in 30 second increments for the duration of the experiment. The samples were heated using a hot-air blower. The temperature was controlled by a thermocouple positioned between the nozzle of the hot-air blower and the sample capillary. The reaction mixture and glass wool were carefully mixed in a 50:50 wt% ratio. The mixture was

loaded into 1.5 mm quartz capillaries. The capillaries were sealed before the measurement in the case of the reaction without flow. For the flow-through experiments, the open-ended capillaries were mounted in a Norby cell[56]. The dry nitrogen flow was taken directly from the gas bottle through a rotameter. The humid gas flow was prepared by bubbling nitrogen through a saturated $MgCl_2$ salt solution, resulting in 33 % relative humidity at room temperature. The flow rate was in both cases kept constant at approximately 10 ml min^{-1}. The XRD data were analysed using the Rietveld method[57,58], as implemented in the Topas software package (Bruker AXS). Literature crystal structures were used for ZIF-8[25] and LT-HmIM[59]. The phase fractions were quantified using a modified version of the O'Connor and Raven external standard method[60].

Lift-off patterning. Wafers for lift-off patterning were prepared as follows. Silicon wafers were dried on a hot-plate at 190 °C for 10 min and then coated with AZ positive tone resist. The 1.2 µm thick resist layer was produced by spin coating the wafer with AZ5214E resist at 3000 rpm, followed by soft baking on a hot-plate at 100 °C for 1 min. The photo resist was then exposed to UV through a soda-lime mask on a MJB4 (Suss MicroTec) and developed in AZ400K developer, 1:4 diluted with DI water. The wafers were subsequently washed with water and dried under nitrogen flow. Zinc oxide (20 nm) was deposited by reactive RF sputtering (zinc target, oxygen plasma atmosphere). The vapour-solid reaction was performed for 30 min at 100 °C. The photoresist lift-off was subsequently conducted by sonication of the wafers in acetone at 40 °C for 10 minutes.

PDMS pillars. PDMS pillars were made by means of soft lithography. A silicon mold was prepared using Bosch processing (2 µm diameter, 5 µm pillar height and 2 µm inter pillar distance). The silicon mold was then vapour-treated with an anti-sticking layer (Trichloro(1H,1H,2H,2H-perfluorooctyl)silane). PDMS elastomer 184 from Dow Corning was prepared by mixing the base resin with its reticulating agent in 10:1 ratio and outgassed for 30 min in a vacuum jar; the mixture was then poured on the mold and outgassed for 30 min more in order to provide a careful filling of the cavities. After curing at 90 °C for 30 min, 1x1 cm^2

patches were cut with a razor blade and gently peeled off. The pillars were coated with 3 nm of zinc oxide by ALD and with ZIF-8 by vapour-solid reaction for 30 min at 100 °C.

References

52. Klug, H. P. & Alexander, L. E. *X-Ray Diffraction Procedures: For Polycrystalline and Amorphous Materials, 2nd Edition*. (1974).

53. Schindelin, J. *et al.* Fiji: an open-source platform for biological-image analysis. *Nat. Methods* **9,** 676–682 (2012).

54. Nečas, D. & Klapetek, P. Gwyddion: an open-source software for SPM data analysis. *Cent. Eur. J. Phys.* **10,** 181–188 (2012).

55. Willems, T. F., Rycroft, C. H., Kazi, M., Meza, J. C. & Haranczyk, M. Algorithms and tools for high-throughput geometry-based analysis of crystalline porous materials. *Microporous Mesoporous Mater.* **149,** 134–141 (2012).

56. Norby, P. In-Situ Time Resolved Synchrotron Powder Diffraction Studies of Syntheses and Chemical Reactions. *Mater. Sci. Forum* **228-231,** 147–152 (1996).

57. Rietveld, H. M. A profile refinement method for nuclear and magnetic structures. *J. Appl. Crystallogr.* **2,** 65–71 (1969).

58. Young, R. A. *The Rietveld Method (International Union of Crystallography Monographs on Crystallography)*. (1993).

59. Hachuła, B., Nowak, M. & Kusz, J. Crystal and molecular structure analysis of 2-methylimidazole. *J. Chem. Crystallogr.* **40,** 201–206 (2010).

60. O'Connor, B. H. & Raven, M. D. Application of the Rietveld Refinement Procedure in Assaying Powdered Mixtures. *Powder Diffr.* **3,** 2–6 (2013).

Acknowledgements

The authors are grateful to the Agency of Innovation by Science and Technology (IWT) for support in SBO project MOFShape. I.S. thanks Research Foundation Flanders (FWO) for a PhD fellowship. R.A. is grateful to KU Leuven for a starting grant. The authors thank imec for support. In particular, the ESTORE team is acknowledged for their assistance in providing the substrates and the imec MCA department for TEM and TOF-SIMS measurements. D.D.V. is grateful to the Belgian Science Policy (BELSPO) for support in IAP project 7/05 and to KU Leuven for CASAS Methusalem funding. S.D.F. is grateful to the European Research Council (ERC) for funding (Grant Agreement No. 340324).

Author contributions

I.S. and R.A. conceived and designed the experiments. I.S. carried out and analysed all film deposition and characterisation experiments. M.J.S., P.F., and R.A. designed and conducted the X-ray diffraction measurements. M.J.S. and I.S. analysed the X-ray diffraction data. H.V.G. and W.V. conducted the atomic force microscopy experiments. G.G. and P.F. designed and manufactured the photolithography and soft lithography patterned substrates. The manuscript was primarily written by I.S. and R.A., with the input of all authors.